Hindawi
Wireless Communications and Mobile Computing
Volume 2023, Article ID 9846815, 1 page
https://doi.org/10.1155/2023/9846815

Retraction

Retracted: Application of Optical Fiber Sensing Technology in Permeability Test of Three-Dimensional Physical Model of Medium and Long-Distance Diversion Tunnel

Wireless Communications and Mobile Computing

Received 8 August 2023; Accepted 8 August 2023; Published 9 August 2023

This article has been retracted by Hindawi following an investigation undertaken by the publisher [1]. This investigation has uncovered evidence of one or more of the following indicators of systematic manipulation of the publication process:

(1) Discrepancies in scope
(2) Discrepancies in the description of the research reported
(3) Discrepancies between the availability of data and the research described
(4) Inappropriate citations
(5) Incoherent, meaningless and/or irrelevant content included in the article
(6) Peer-review manipulation

The presence of these indicators undermines our confidence in the integrity of the article's content and we cannot, therefore, vouch for its reliability. Please note that this notice is intended solely to alert readers that the content of this article is unreliable. We have not investigated whether authors were aware of or involved in the systematic manipulation of the publication process.

Wiley and Hindawi regrets that the usual quality checks did not identify these issues before publication and have since put additional measures in place to safeguard research integrity.

We wish to credit our own Research Integrity and Research Publishing teams and anonymous and named external researchers and research integrity experts for contributing to this investigation.

The corresponding author, as the representative of all authors, has been given the opportunity to register their agreement or disagreement to this retraction. We have kept a record of any response received.

References

[1] Z. Xu, G. Zhang, X. Chen, L. Yao, G. Chen, and F. Wang, "Application of Optical Fiber Sensing Technology in Permeability Test of Three-Dimensional Physical Model of Medium and Long-Distance Diversion Tunnel," *Wireless Communications and Mobile Computing*, vol. 2022, Article ID 7931914, 10 pages, 2022.

Hindawi
Wireless Communications and Mobile Computing
Volume 2022, Article ID 7931914, 10 pages
https://doi.org/10.1155/2022/7931914

Research Article

Application of Optical Fiber Sensing Technology in Permeability Test of Three-Dimensional Physical Model of Medium and Long-Distance Diversion Tunnel

Zhijing Xu, Guanghui Zhang, Xiaoming Chen, Liangxue Yao, Guangyao Chen, and Fei Wang

PowerChina Guiyang Engineering Corporation Limited, Guiyang, Guizhou 550000, China

Correspondence should be addressed to Zhijing Xu; 202006000162@hceb.edu.cn

Received 17 July 2022; Revised 22 August 2022; Accepted 3 September 2022; Published 12 September 2022

Academic Editor: Aruna K K

In order to accurately simulate the dynamic change law of seepage field during construction, this paper proposes the application of optical fiber sensing technology in the permeability test of three-dimensional physical model of medium and long-distance headrace tunnel. This paper introduces the principle of optical fiber sensing, analyzes and compares the application advantages of optical fiber and general electrical signal sensing in the safety monitoring of long-distance diversion tunnel. Taking the safety monitoring of a 16# long tunnel of a diversion project as an example, the selection of monitoring sections, monitoring items, and the layout and networking of monitoring instruments are studied. In addition, combined with the tunnel project, the physical simulation of the construction process of the deep buried headrace tunnel under high seepage pressure is carried out, and the water pressure automatic control water supply system and the discrete flower tube seepage generation system are designed and manufactured to realize the high simulation of the seepage field. The seepage and evolution law in the surrounding rock of headrace tunnel during dynamic construction are calculated and analyzed. The test results show that the maximum external water pressure of the headrace tunnel is 15 MPa, which is equivalent to 1500 m head pressure, and the similar scale of head pressure is 100. Therefore, taking 15 m constant head water supply pressure for simulation calculation, the excavation of the tunnel is 120 cm, and the two-dimensional seepage of the vertical section of $Z = 91$ cm. The seepage flow of the two sides of the tunnel is large, and the contour of the hydraulic gradient is dense. The coordinates are 0.7 m, 2.090 m, and 0.9 m. This point in the original rock mass is located at the same elevation point of the four headrace tunnels and directly below the model exploratory tunnel. The head pressure is 1.40 m, and the corresponding prototype point pressure head is 140 M. During construction, such a high external water pressure is a great safety hazard. *Conclusion*. The test conclusion provides a theoretical basis for the seepage prevention construction technology design of the headrace tunnel and is of great significance to the long-term stability, safety evaluation, and prediction of the headrace tunnel.

1. Introduction

With the pace of China's reform and opening up, the booming market economy has put forward newer and higher requirements for large-scale civil and water conservancy projects, which has also greatly promoted the expansion of infrastructure construction and the rapid development of underground diversion tunnel projects. In response to the sustainable development of the economy and the saving of construction land, as well as the growth of the demand for renewable energy, the construction of infrastructure has gradually shifted from the above ground space to the underground space, which has also greatly promoted the development of water conservancy and hydropower engineering construction [1, 2].

FBG Optical fiber sensor components are one of the mechanical sensor components that have developed rapidly in the recent period. Because it has many unique advantages over traditional mechanical sensor components, it has broad application prospects in the fields of optical fiber communication,

optical fiber sensing, optical computing, and optical information processing. FBG Optical fiber sensor is developed by using its own photosensitive characteristics. The so-called photosensitive characteristic in optical fiber refers to the characteristic that the refractive index of optical fiber will change correspondingly with the spatial distribution of light intensity when the laser passes through the hybrid optical fiber (this phenomenon is also known as the effect of photoinduced refractive index change). The wavelength of the reflection or transmission peak of the grating is related to the modulation period of the refractive index of the grating and the refractive index of the fiber core, which causes the change of the wavelength of the reflection or transmission peak of the fiber grating. This is the basic working principle of the FBG fiber sensor. Therefore, temperature and strain are the most basic physical quantities that fiber Bragg grating can directly sense and measure. These two physical quantities are the sensing basis of other physical quantities, and the sensing of other physical quantities are indirectly derived from the strain and temperature sensing of fiber Bragg grating [3]. The emergence of FBG Optical fiber sensor has changed the traditional thinking of practitioners in the field of optical fiber technology, making its application in other engineering fields become common and injecting new impetus into the development and application of optical fiber sensing technology. As shown in Figure 1:

2. Literature Review

The sensor is the central device throughout the safety monitoring system. The development process of the sensor also reflects the development process of the safety monitoring of the headrace tunnel. Sensor technology came out in the 1950s, and its development is closely related to the progress of science and technology. The development of sensors applied to the safety monitoring of headrace tunnel projects has roughly gone through three stages, first the differential resistance sensors used, then the vibrating wire sensors widely used and even still active in the sensor industry, and finally the relatively developed fiber Bragg grating sensors. Throughout the development process of sensors, sensors are developing in the direction of light weight, fast response, integration, and intelligence. Fiber Bragg grating sensors can not only meet the basic requirements of data acquisition, processing, and analysis, but also carry out error compensation and corresponding logical thinking and conclusion judgment on the collected data. The United States has been in the leading position in the world in the research and development of sensors. At present, the United States, Germany, Canada, and the United Kingdom are committed to the research of FBG demodulation system, while China has a large gap with developed countries due to the late start of sensor technology.

Yin et al. applied FBG sensors to tunnels and other buildings for long-term monitoring and proposed a new method to maintain structures on this basis [4]. Jiang et al. studied the elastoplastic response of tunnel lining concrete monitored by FBG sensor in an earthquake area [5]. Naguib et al. used FBG sensing technology to monitor the strain of the secondary lining of Tunnel 3 in Bainijing [6]. Kumar et al. summarized some problems often encountered by FBG sensors in the monitoring of tunnel projects under construction such as packaging protection, temperature compensation, and system integration, and the FBG sensor is applied to the safety monitoring of a tunnel under construction to realize the real-time monitoring of the arch internal force, concrete stop strain, and temperature of spray concrete during tunnel excavation. From the later monitoring data, the FBG sensor has stable performance and small system error [7]. Ismail et al. designed a long-distance FBG settlement pipe monitoring system for subway tunnel settlement monitoring to realize the online monitoring of subway tunnels in normal operation. Fiber Bragg grating sensors are mainly laid on the surface of steel pipes to make FBG settlement pipes, and multiple FBG settlement pipes are combined through sleeves to connect long-distance FBG settlement pipes. At the same time, the installation scheme is designed in detail, and a long-distance FBG settlement pipe monitoring system is built, which has been successfully applied to the settlement monitoring of Shanghai Metro Line 8 [8]. Wang et al. installed optical fiber displacement sensors on the tunnel rock wall to monitor the stress of surrounding rock during tunnel construction [9]. Kerimov et al. installed the fiber Bragg grating sensor on the carbon fiber cable of lucerne bridge, and the strain measurement range reached 8000 [10]. Yang et al. proposed solutions and ideas for the packaging protection, temperature compensation, and system integration of fiber Bragg grating sensors in tunnel engineering monitoring [11]. Zhang et al. applied an embedded FBG strain sensor to the headrace tunnel to study the strain of lining concrete. For projects with long tunnels or long-distance signal transmission, it is an effective choice to use fiber Bragg grating sensors for safety monitoring [12].

The safety monitoring of hydraulic tunnels often relies on vibrating wire and differential resistance instruments. Limited by the principle of electrical instruments, class 2 instruments can no longer meet the safety monitoring needs of long tunnels, and the optical fiber sensing technology points out the direction to solve the problem of signal acquisition and transmission in such tunnels. Using optical fiber transmission, a large number of long-distance data transmissions can be completed, and the fiber Bragg grating sensor is a passive device, which can adapt to the complex environment such as high humidity and strong corrosion underground. Therefore, the optical fiber sensing technology can meet the safety monitoring needs of long-distance headrace tunnels. At present, there are a few application examples in China [13]. The research on optical fiber sensing technology in China started a little later than that in the world, and its application in engineering is also relatively late. It is lack of experience in the use of long-distance headrace tunnel engineering monitoring.

For the numerical analysis of large-scale headrace tunnel projects with different geological and in situ stress conditions, different numerical methods will give different results. Because the seepage physical model is a real physical entity, it can truly reflect the spatial relationship between geological structure and engineering structure under the condition of basically meeting the similarity principle and can accurately simulate the dynamic change law of seepage field in the

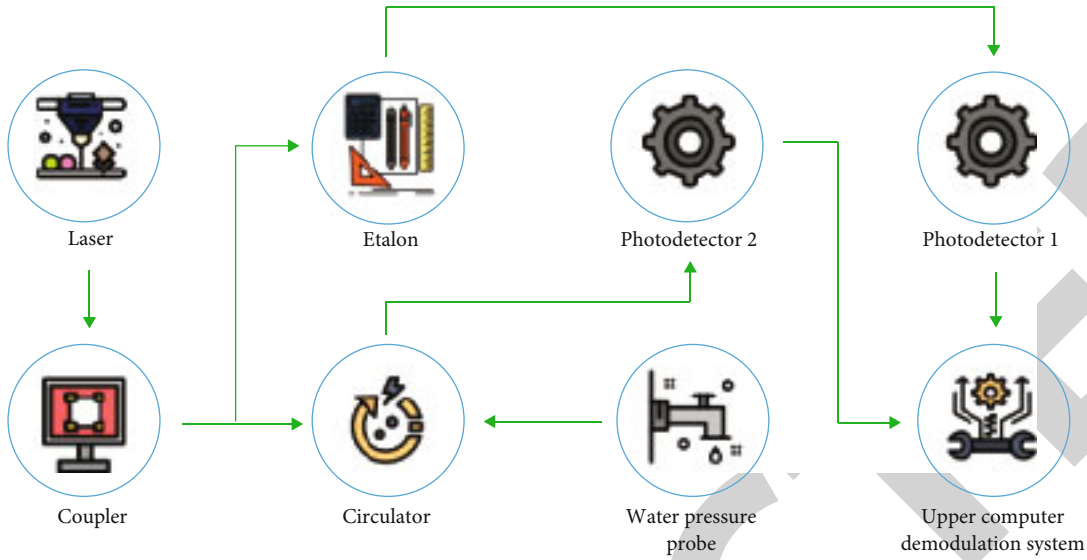

Figure 1: Three-dimensional physical model of optical fiber sensing technology in medium and long distance headrace tunnel.

construction process. Secondly, various numerical analysis results can also be verified through physical model tests, which is undoubtedly of great significance to large or super large rock mass structural engineering. In this paper, the physical simulation of the whole excavation process of four headrace tunnels under the conditions of strong seepage pressure, high buried depth, and high ground stress of a hydropower station is carried out, and the seepage field and its evolution law during the construction process are studied.

3. Research Methods

3.1. Optical Fiber Sensing Principle. The full name of optical fiber is "optical fiber". The optical fiber used in geotechnical engineering generally has complex surrounding and on-site construction and installation environment, and it is usually protected by several layers of protective structures. Transmission optical fibers commonly used in engineering have thick coating and small core diameter. The standard cladding diameter of a single optical fiber is 125 μm. The diameter of the plastic coating is about 250 μm. The coating structure of optical fiber includes buffer layer and coating.

The basic transmission principle of optical fiber is the total reflection of light, as shown in Figure 2. Once the light enters the optical fiber, the light enters the optical fiber core from the beginning of the optical fiber. The information transmission principle of the optical fiber is based on the reflection phenomenon of light, but the refractive index of the optical fiber core is inconsistent with that of the outer cladding of the optical fiber [14]. When the light enters the fiber core, part of the light will be refracted in the fiber, so the light beam entering the fiber will lose part, resulting in the reduction of the transmission effect of the fiber. Therefore, in practical operation, users will first adjust the angle of light entering the optical fiber. Once this angle reaches a certain critical value, the light entering the optical fiber will not refract again, and the light beam will advance completely inside the optical fiber by the reflection of light, so as to improve the transmission efficiency.

3.2. Sensing Principle of Fiber Bragg Grating Sensor. There are many types of fiber Bragg grating. If the fiber Bragg grating is divided simply from the structure, the fiber Bragg grating can be divided into periodic grating and aperiodic grating. Fiber gratings with periodic structure can be divided into two sub categories, namely, Bragg gratings and transmission gratings, also known as short period gratings and long period gratings [15]. The most widely used grating in practical engineering is Bragg grating, whose English abbreviation is fiber Bragg grating, which is also known as fiber Bragg grating (FBG). Fiber Bragg grating mainly uses ultraviolet light to shoot light into the fiber core. The reflection principle is conditional on the beam. Only the incident light that meets the Bragg diffraction condition can be reflected at the grating, and other light will not be affected. The reflection spectrum has a peak at the central wavelength of FBG.

The refractive index change of the fiber core will form a spatial phase grating in the fiber core. Once we know the refractive index of the fiber and the period of the grating, we can calculate the central wavelength of the grating. Its calculation formula is the following Formula (1):

$$\lambda_B = 2n_{eff}\Lambda, \tag{1}$$

where λ_B-central wavelength of optical fiber (FBG) grating, nm; Λ-grating period; n_{eff}-effective refractive index of fiber core.

The grid spacing of the grating is distributed along the axial direction of the fiber core, and its grid spacing will be affected by many factors. For example, the ambient temperature, the pressure on the optical fiber, etc. Once these external factors such as temperature and pressure change, the refractive index and axial direction of the optical fiber will change, and then the grid distance of the optical fiber will also change, resulting in the wavelength change of the

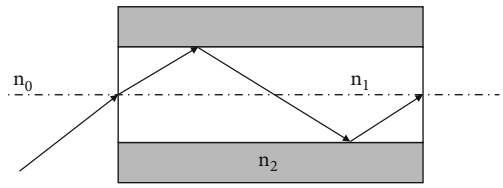

Figure 2: Fiber core structure and light guiding principle diagram.

reflected light [16]. It is found that the relationship between the change of central wavelength of reflection spectrum and temperature T and strain ε is as follows (2):

$$\frac{\Delta\lambda_B}{\lambda_B} = \left(\alpha_f + \xi\right)\Delta T + (1 - P_e)\Delta\varepsilon, \quad (2)$$

where α_f-coefficient of thermal expansion; ξ-thermal optical coefficient; P_e-elastic optical coefficient.

Under certain constant temperature and other specific conditions, without considering the influence of temperature change, Equation (2) is simplified to the following Equation (3):

$$\frac{\Delta\lambda_B}{\lambda_B} = (1 - P_e)\Delta. \quad (3)$$

At this time, the axial stress changes linearly with the change of the central wavelength of the fiber Bragg grating (FBG).

3.3. Application Advantages of Optical Fiber Sensing Technology. The optical fiber used in the project generally requires a large number of channels due to the number of monitoring points. Most of them use multicore optical fiber clusters composed of multiple optical fibers and outer protective layers, namely optical cables. Optical cable transmission and fiber Bragg grating sensor have the following advantages compared with traditional cable transmission and electrical signal instruments: (1) it integrates transmission and sensing, with large amount of transmission data, small attenuation, and long transmission distance; (2) nonmetallic insulating materials are not affected by damp environment, high temperature resistant, corrosion resistant, and suitable for special environments such as underground engineering; (3) optical signal transmission is hardly affected by factors such as light source power, light fluctuation and connection loss, and has good stability; (4) Its small size, light weight, free from electromagnetic noise interference, high transmission quality, and sensing sensitivity; (5) The sensor has high monitoring efficiency, and a single fiber can write multiple gratings with different wavelengths for real-time quasi-distributed monitoring; (6) With good adaptability, simple structure, and small geometric size, it is suitable for embedding inside all kinds of buildings [17].

3.4. Networking Mode of Fiber Bragg Grating. Fiber Bragg grating (FBG) sensing is a quasi-distributed fiber sensing technology, which generally adopts single-end or head and tail end fiber output mode. When both ends are out of fiber, if one end cannot work normally due to damage or destruction, the other end can be connected to replace the measurement. Most fiber Bragg gratings (FBG) work at 1520~1570 nm, and the window range is limited. Therefore, the grating wavelengths written by the same group of sensors cannot be overlapped. If there is overlap, the demodulator cannot receive the reflected light written by the grating in the sensor, resulting in data cannot be read. The number of series parallel fiber (FBG) gratings commonly used in engineering to write strain, and temperature double factors is generally not more than 6, and the number of series parallel fiber (FBG) gratings used under some specific conditions that only write strain single factors is generally not more than 12.

3.5. Safety Monitoring Layout of Long-Distance Headrace Tunnel

3.5.1. Necessity of Safety Monitoring. The adverse geological conditions revealed by the tunnel include surrounding rocks with extremely poor stability, such as quaternary saturated loess like soil, Paleogene (Neogene) extremely soft rock, Presinian gneiss paleo differentiated crust, fault zone, etc.; the stability of surrounding rocks is prominent, which is a key project for the success or failure of engineering construction and operation safety. Therefore, it is particularly important to do a good job in the safety monitoring of the tunnel, pay close attention to the stability of the surrounding rock of the tunnel and the operation state of the building, and ensure the safety and reliability of the tunnel construction and long-term operation.

3.5.2. Safety Monitoring Layout

(1) Layout of Safety Monitoring Section. 16# the focus of tunnel safety monitoring is the stability of surrounding rock. According to the geological conditions revealed by tunnel excavation, it is arranged in representative tunnel sections and key parts such as tunnel sections with poor stability and various adverse geological conditions, shallow buried deep tunnel sections, and tunnel sections with changing water flow conditions. According to the layout principle of safety monitoring, a total of 7 monitoring sections are arranged: saturated soil tunnel body, unconformity contact surface with lithological changes, shallow buried places through valleys, tunnel body faults, shallow buried places at outlets, and changes in water flow conditions. See Table 1 for the layout statistics of sections.

(2) Selection of Main Monitoring Items. The safety monitoring categories of hydraulic tunnels mainly include deformation monitoring, seepage monitoring, stress-strain monitoring, etc. In combination with the permanent monitoring requirements during the operation period of the project, the main monitoring items are determined as follows: monitoring the internal deformation and loosening range of surrounding rock; secondary lining structure joint and crack opening and closing degree monitoring; seepage monitoring; stress and strain monitoring of tunnel surrounding rock and supporting lining structure [18].

Table 1: Statistics of tunnel safety monitoring section layout.

Monitoring section number	Tunnel stake number location	Typical tunnel section characteristics
1	0 + 500	Saturated loess soil tunnel body
2	0 + 950	Saturated loess soil tunnel body
3	3 + 190	Unconformity interface between Lishi loess and silty mudstone
4	8 + 400	Shallow buried part of the valley with low rock strength of the tunnel
5	12 + 225	Unconformity contact surface between glutenite and gneiss
6	13 + 125	F2 fault of tunnel body
7	20 + 490	Shallow burial at the tunnel outlet and changes in water flow conditions

(3) Layout of Safety Monitoring Instruments. According to the construction conditions of the tunnel and the main items to be monitored, combined with the stress conditions of the tunnel transverse lining structure, it is arranged near the maximum stress bending moment and deformation of the tunnel, that is, the top arch crown, the arch foot close to the side bottom arch, and the bottom of the bottom arch. The measuring points of each monitoring section are arranged on the cross section. The monitoring instruments mainly arranged are multipoint displacement meter (m), embedded joint meter (J), surface joint meter (J), osmometer (P), earth pressure meter (E), strain gauge (s), stress free meter (n), and reinforcement meter (R). See Table 2 for the monitoring items and monitoring instrument statistics.

3.5.3. Monitoring Section Networking. 16# the tunnel trunk adopts 48 core optical cables. Each section in the tunnel uses optical fiber couplers to connect branch optical fibers, and all instruments in the same section are networked. Through the trunk optical cables, long-distance transmission is realized, which is led to the field observation station at the entrance of the tunnel, connected to the demodulator, and data interpretation is realized before transmission outside the tunnel [19]. Each section is equipped with 27 optical fiber (FBG) grating sensors, all of which are fiber outgoing at both ends. The series networking is adopted, and the reserved interface is led out of the tail fiber at the end. Among them, the multipoint displacement meter, reinforcement meter, and stress meter are arranged in the closed underground rock mass or poured in the lining concrete. There is no influence of high temperature in the underground environment. The surrounding medium of the sensor is single, and the sensing temperature and temperature transmission amplitude in the same medium are very small. The fiber Bragg grating sensor with single strain factor is used; while joint gauges, osmometers, earth pressure gauges, and stress free gauges are mainly arranged between the rock mass and the primary support, between the primary support and the lining concrete, or on the outer surface of the lining concrete.

3.6. Basic Principle of Similarity and Selection of Model Materials

3.6.1. Basic Principle of Similarity. The design of model test and the selection of basic parameters of model are the first step of model test, and also one of the keys to determine whether the model test is successful. This model test adopts the normal model design. Considering the actual project size and the size of laboratory equipment, the operability of excavation simulation and the simplification of conversion between similar physical quantities, the basic parameter scale of the model is determined as follows:

(1) Geometric scale: $C_L = L_p/L_m = 100$;

(2) Bulk density scale: $C_\gamma = \gamma_p/\gamma_m = 1$;

(3) Stress scale: $C_\sigma = \sigma_p/\sigma_m = C_F/C_L^2 = 100$;

(4) Permeability coefficient scale: $C_k = K_p/K_m = 0.1$.

Physical quantities with the same dimension as the stress have similar scales with the stress, that is, the similar scales of elastic modulus, shear modulus, compressive strength, tensile strength, and cohesion of the material are all 100:

$$C_E = C_G = C_{R_c} = C_{R_t} = C_c = 100. \quad (4)$$

The similar scale of physical quantities such as strain, Poisson's ratio, and internal friction angle of dimension one is 1, that is

$$C_\varepsilon = C_\mu = C_\varphi = 1. \quad (5)$$

3.6.2. Model Material Selection. NIOS (natural iron ore sand) geomechanical model material is used as the model material. NIOS model material is composed of magnetite concentrate powder, river sand, binder (gypsum or cement), mixing water, and additives [20]. The density simulation range of NIOS geomechanical model material is $2.65 \sim 3.00\,g/cm^3$. The proportion range of the main components magnetite powder and natural river sand is $(8.5 \sim 9.5) : (1.5 \sim 0.5)$. Gypsum or cement can be added according to the specific situation, which generally accounts for $1 \sim 3\%$ of the total mass of the model material.

3.7. Transformation of Test Bench and Design of Seepage System

3.7.1. Seepage Generation on Test Bench. The groundwater in the original rock engineering area is enriched and the maximum seepage pressure is 15 MPa. In order to simulate the groundwater, the inner space surrounded by the original test bench is divided into three spaces. The lower part of the

Table 2: Statistics of tunnel monitoring items and monitoring instruments.

Monitoring category	Monitoring items	Monitoring instrument	Number of instruments/piece
Deformation monitoring	Monitoring of surrounding rock deformation and opening and closing of joints and cracks	Multipoint displacement meter (M)	3
		Embedded joint meter (J)	2
		Surface joint meter (J)	4
Seepage monitoring	Osmotic pressure monitoring	Osmometer (P)	2
Stress-strain monitoring	Stress and strain monitoring of tunnel surrounding rock and supporting lining structure	Earth pressure gauge (E)	3
		Strain gauge (S)	4
		Stress free gauge (N)	1
		Reinforcement meter (R)	8
Total			27

space on both sides is used as a water tank to store pressurized water for the convenience of supplying water to the model material. The steel plate on the upper part of the water tank on the side of the model is reinforced and supported by channel steel. In order to simulate the seepage of rock mass with high simulation degree, an automatic pressurization control system is designed and manufactured. The water in the water tank is pressurized water, which is connected with the flower tube embedded in the upper part of the model material through the water supply pipe. Each small hole on the flower tube is used as the source of seepage to continuously and stably provide a certain pressure of water to the model material. The maximum water pressure in the water conveyance tunnel project area is 15 MPa, and the underground water pressure to be simulated in the physical model is 0.15 MPa. This pressure is achieved by continuously and stably inflating and pressurizing the free water surface in the water tank.

In order to ensure the authenticity of seepage simulation in the model and meet the dynamic changes of seepage field, an automatic pressurized water supply system and a distributed seepage pipe network system were developed. The automatic pressure control system is set on the top of the water supply tank to realize the automatic adjustment and water supply of the water level in the tank according to the change of the water pressure in the water tank. Each water tank is supplied upward by two water supply mains, each water supply mains is connected with 16 branch pipes, and a total of 32 branch pipes are connected with the flower pipes embedded in the model material through the small holes of the lateral steel plate to supply water to the model, ensuring the authenticity of the seepage field in the model. In order to prevent the floret from blocking, wrap the floret around with hemp yarn.

3.7.2. Test the Antiseepage of Enclosure Steel Plate and Top Loading Device. One of the key technical problems of the model test is the seepage prevention of the five steel plates at the bottom, front, rear, left and right of the model, and the upper combined steel barrel. This problem faces two challenges: first, the steel plate structure of the test bench maintenance is large, and there are many data acquisition lines and movable displacement transfer rods that need to be extended through the holes on the steel plate; second, the pressurization system at the top of the model is a composite loading body of assembled steel sleeve and air bag, which is difficult to prevent seepage in order to solve the antiseepage problem of the steel plate around the model and the holes of various data lines on it, and the waterproof problem of high-precision multipoint displacement meter [21]. The test successfully developed the data line through the steel plate hole rubber fixed antiseepage technology, the displacement transmission rod and the sleeve filled with grease antiseepage technology, the sleeve and the copper pipe fixed on the steel plate with rubber pad water stop technology, and the assembled steel sleeve with rubber strip antiseepage technology. These antiseepage techniques ensure the authenticity of seepage field simulation.

The displacement of a certain point in the model is transmitted through the steel rod sleeved in the fine steel casing, and the gap between the casing and the transfer rod will produce seepage. Therefore, filling the gap between the steel casing and the displacement transfer rod with viscous grease can prevent not only the infiltration of water but also ensure the free sliding of the transfer rod and ensure the normal collection of displacement. When the displacement transmission and its casing pass through the maintenance steel plate, it is wrapped with rubber or hemp wire outside the casing to prevent pressurized water leakage in the model.

The top of the model material is covered and sealed with an assembled steel sleeve barrel. The steel sleeves are connected with channel steel. An air bag is placed under the steel sleeve. The steel sleeve is pressurized with a jack and inflated in the air bag. The air bag exerts a reverse pressure on the top of the model material. The measuring instrument rod passes through the channel steel connecting the two steel sleeves. Attention should be paid to sealing water between the holes.

3.8. Layout and Embedding of Osmometer. In this test, 10 osmometers were buried in the model material to measure the change of water pressure in the model material and around the tunnel during the excavation of the headrace tunnel. Before burying the osmometer, first drill holes in

Table 3: Parameter values of model materials.

Material type	Bulk density γ /(kN·m^{-3})	Modulus of elasticity E/GPa	Poisson's ratio μ	Permeability coefficient k/(cm·s^{-1})
Model material	27.7	0.19	0.23	8.19×10^{-5}
Prototype material	27.7	18.50	0.28	8.32×10^{-4}

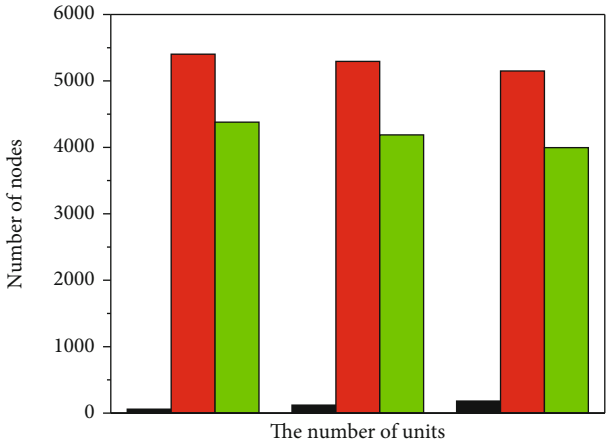

Figure 3: Mesh number of model calculation unit under each excavation footage.

Table 4: Seepage flow of each tunnel under 15 m head pressure (m^3/d).

Hole number	Excavation 60 cm	Excavation 120 cm	Excavation 182 cm
1	0.87	1.29	1.50
2	0.36	0.48	0.48
3	0.37	0.46	0.49
4	0.85	1.29	1.50
Exploratory cave	1.17	0.68	0.49

the design position with a drill and evenly lay 2 ~ 3 cm thick medium and fine sand at the bottom of the hole, then slowly put the osmometer into the hole, fill the model material in the upper part of the osmometer, and gently tamp it.

The calculation formula of water seepage pressure is the following Formula (6):

$$P = K'\left(f_0^2 - f_i^2\right), \tag{6}$$

where P is the osmotic pressure (MPa); K' is the calibration coefficient (MPa/Hz^2), which is provided by the manufacturer; f_0 is the initial reading of the osmometer (Hz); f_i refers to each reading (Hz) of the osmometer.

4. Result Analysis

4.1. Calculation Parameters. It is difficult to control and realize the seepage simulation of the model material in the indoor physical model test. In order to accurately simulate the initial seepage field and the change law of the seepage field during the excavation of the model tunnel in the indoor physical simulation test, control the seepage flow of each tunnel during the excavation process and adjust the water pressure value in the water supply box; a preliminary calculation of the seepage evolution law in the model material should be carried out before the test [22]. In this model test, the distribution length of class III marble and class III sand slate of Baishan formation along the headrace tunnel accounts for 70% of the total length. The physical model test mainly simulates this kind of rock mass, and the parameter values of model materials are shown in Table 3.

4.2. Seepage Calculation Model. Commonly used seepage media calculation models: continuous media seepage model, porous continuous media seepage model, and fractured continuous media seepage model. In this paper, the seepage calculation theory of three-dimensional physical entity model adopts the seepage theory of porous media, and its essence can be explained by mathematical models, that is, some equations or equations are used to describe the basic characteristics, internal characteristics, and the restriction relationship of external conditions on seepage movement in porous media [23].

For the porous anisotropic material model in accordance with Darcy's law, when the coordinate axis direction is consistent with the seepage axis, the three-dimensional seepage problem can be reduced to the definite solution problem of the following Formula (7), (8), (9), and (10):

$$\frac{\partial}{\partial x}\left(k_x \frac{\partial H}{\partial x}\right) + \frac{\partial}{\partial y}\left(k_y \frac{\partial H}{\partial y}\right) + \frac{\partial}{\partial z}\left(k_z \frac{\partial H}{\partial z}\right) = \mu_s \frac{\partial H}{\partial t}. \tag{7}$$

Initial conditions:

$$H|_{t=0} = f_0(x, y, z, 0)\ (\text{在}\Omega\text{内}). \tag{8}$$

Head boundary:

$$H|_{\Gamma_1=0} = f_1(x, y, z, t)\ (\text{在}\Gamma_1\text{内}). \tag{9}$$

Flow boundary:

$$k_n \frac{\partial H}{\partial n}\bigg|_{\Gamma_2} = f_2(x, y, z, t)\ (\text{在}\Gamma_2\text{内}), \tag{10}$$

where Ω is the calculation seepage area, that is, the research area composed of boundary curves Γ_1 and Γ_2; Γ_1

Table 5: Seepage pressure at each characteristic point under 15 m head (excavation 120 cm).

Osmometer no	Feature point number	Feature point coordinates/m			Seepage pressure at characteristic points/m	Estimated seepage water pressure at corresponding points of prototype/m
		x	y	z		
1	1	0.7	2.090	0.6	2.04 (2.02)	204
2	2	0.7	2.090	0.9	1.40 (1.33)	140
3	3	0.7	2.090	1.3	1.82 (1.78)	182
4	4	0.7	2.090	1.5	3.30 (3.20)	330
5	5	0.7	2.090	1.8	4.38 (4.13)	438
6	6	0.7	2.090	2.2	5.15 (5.12)	515
7	7	0.7	2.705	0.9	1.94 (1.87)	194
8	8	0.7	3.305	0.9	5.55 (5.41)	555
9	9	0.7	3.305	0.9	8.79 (8.67)	879
10	10	0.7	3.920	0.9	11.94 (11.89)	1 194

Note: the measured values are in brackets.

and Γ_2 are boundary curves of known head value and flow value, respectively; n is the normal direction of the boundary curve; $f_0(x, y, z, 0)$ is the initial head value of each point in the calculation area; $f_1(x, y, z, t)$ is the known head value on Γ_1; F2 is the known flow value on Γ_2.

In this paper, the mathematical model is described as follows (11):

$$\left.\begin{aligned} &\frac{\partial}{\partial x}\left(k_x\frac{\partial H}{\partial x}\right)+\frac{\partial}{\partial y}\left(k_y\frac{\partial H}{\partial y}\right)+\frac{\partial}{\partial z}\left(k_z\frac{\partial H}{\partial z}\right)=0\\ &H|_{\Gamma_1=0}=f_1(x,y,z,t)\left(\text{在 }\Gamma_1\text{ 内}\right)\end{aligned}\right\}. \tag{11}$$

4.3. Seepage Calculation of Model Body. The actual physical model size is 418 cm ×182 cm ×240 cm (length × wide × Height), using three-dimensional model for calculation, along the excavation direction is the x-axis, the vertical excavation direction is the y-axis, the vertical upward is the z -axis, and the coordinate origin is at the northeast corner of the bottom of the model. Before excavation, the circular blocking plate at the end of the model tunnel is removed first, and then the excavation is carried out according to the established test plan. The author calculates the excavation conditions of 60120182 cm (all excavation). The calculation element is hexahedral element, and the corresponding element and grid number are shown in Figure 3. The external water head on the side of the model is a local constant water head, which forms a stable seepage in the model body. Only with the change of the excavation footage of the small cavern, the seepage field changes accordingly. The calculated water head is 15 m. The excavation of four model tunnels is carried out synchronously, and the calculated excavation footage is 60, 90182 cm, respectively. The single tunnel in the upper part of the physical model simulates the exploratory tunnel in the actual project, which is completed before the excavation of the four headrace tunnels. The tunnel has been completed before the seepage calculation, and the calculation adopts the seepage special program [24].

4.4. Seepage Flow of each Tunnel. The maximum external water pressure of the headrace tunnel is 15 MPa, which is equivalent to 1500 m head pressure. The similar scale of head pressure is 100. Therefore, the 15 m constant head water supply pressure is taken for simulation calculation. The seepage flow of each tunnel under different excavation footage is shown in Table 4. The seepage generation system continuously supplies water to the model material to form a seepage field. The seepage field changes dynamically during the excavation of the tunnel. During the actual construction, we must grasp the evolution law of the seepage field to provide basis for construction drainage and tunnel lining support.

It can be seen from Table 4 that with the advance of excavation, the seepage flow in the exploration tunnel gradually decreases, while the seepage flow in the diversion model tunnel gradually increases.

Seepage field when four model tunnels are simultaneously excavated for 120 cm under 15 m constant head (corresponding to 1500 m prototype head pressure). The water head contour within a certain range of the tunnel axis elevation is relatively dense, and the water pressure gradient changes greatly, indicating that the seepage pressure acting on the rock around the tunnel is greater than other parts during the excavation process. The seepage flow at the excavation face is larger than that at the excavated part, and timely drainage during the construction period is necessary.

The excavation of the cavern is 120 cm, and the two-dimensional seepage flow of the vertical section of $Z = 91$ cm . The seepage flow of the tunnels on both sides is large, and the contour lines of the hydraulic gradient are relatively dense.

4.5. Seepage Analysis. The measured and calculated head pressure of each monitoring characteristic point when the headrace tunnel is excavated 120 cm is shown in Table 5. By analyzing the data in Table 5, the calculated and measured seepage pressure values of each monitoring characteristic point are basically consistent [25]. The head pressure at the corresponding point of the prototype rock mass can be inferred from the model head pressure value according to

the similar scale. Although the external water pressure of the rock mass surrounding the excavation of the cavern decreases a lot, it is still relatively large, such as feature point 2, whose coordinates are (0.7 m, 2.090 m, and 0.9 m). This point in the original rock mass is located at the same elevation point of the four headrace tunnels and directly below the model exploratory tunnel. The head pressure is 1.40 m, and the corresponding prototype point pressure head is 140 M. During construction, such a high external water pressure is a major safety hazard.

When there are no large faults, fissures, and other structures or karst caves along the tunnel, the seepage field is basically stable and symmetrically distributed under a certain head pressure. The water pressure isoline of the surrounding rock of the headrace tunnel is dense; the water pressure gradient changes greatly, and the seepage at the excavation face is relatively serious. It is required to strengthen drainage during the construction process and take comprehensive technical measures of blocking, drainage, and interception to eliminate the adverse effects of high seepage pressure and large seepage flow on the construction. Measures such as surrounding rock grouting, pumping and drainage in the tunnel, and drainage galleries arranged outside the tunnel can be adopted for treatment.

In order to solve the continuous effect and long-term adverse effect of high external water pressure on the lining during the operation period of the project, materials with certain water permeability can be selected as the lining layer, and drainage holes are set on the lining layer at intervals to ensure the normal working state of the lining.

5. Conclusion

Optical fiber sensing technology effectively solves the problem of long-distance signal transmission in underground engineering. In recent years, it has been widely used in the safety monitoring of long tunnels such as railways and highways, but domestic projects are rarely used in the environment of long-term water and high humidity tunnel. After the embedding of various optical fiber (FBG) grating sensors in the tunnel of the project is completed, the survival rate reaches more than 99%, the environmental adaptability is strong, and the practical application effect of the project is good. The working state of each equipment is tested at the site station at the entrance of the tunnel, which can meet the measurement requirements of the design. However, the fiber itself is fragile, and it is easy to break under bending, steering, coiling, and external force touch. Therefore, its installation still needs professionals, and the technical requirements are high. Due to the technical advantages, unique sensing mode, and environmental adaptability of optical fiber sensing, it will be widely used in the safety monitoring of long-distance tunnels in hydraulic engineering.

The formation and evolution of seepage field in the whole process of headrace tunnel excavation under high ground stress, high buried depth, and strong seepage pressure are studied by using the method of three-dimensional physical model test and numerical analysis, and the following research results are obtained:

(i) The test-bed was reformed, and the water pressure automatic control system and the discrete perforated pipe seepage generation system were designed and manufactured, which realized the high physical simulation of seepage field

(ii) The sealing and seepage prevention of various data acquisition rods and lines passing through the test box, and the seepage prevention of the multipoint displacement meter itself are studied, and several seepage prevention techniques and measures are proposed to ensure that the generation and simulation of seepage field can accurately reflect the change law of rock seepage in the actual engineering area

(iii) Comparison and analysis of test data and numerical calculation results of three-dimensional physical model. The conclusions and suggestions with certain reference value for engineering design and construction are given

Data Availability

The data used to support the findings of this study are available from the corresponding author upon request.

Conflicts of Interest

The authors declare that they have no conflicts of interest.

References

[1] X. Fu, S. He, J. Du, X. Wang, and T. Ge, "Variations in naturalistic driving behavior and visual perception at the entrances of short, medium, and long tunnels," *Journal of Advanced Transportation*, vol. 2020, Article ID 7630681, 16 pages, 2020.

[2] Y. Yang, Z. Tan, Z. Jiang, J. Yao, and Z. Hu, "Influences of uncertainties to the generation feasible region for medium- and long-term electricity transaction," *Global Energy Interconnection*, vol. 3, no. 6, pp. 595–604, 2020.

[3] G. Galiqi, B. Luan, A. Pesha, A. Koni, and B. Shega, "Application of the monti procedure in adult continent cutaneous urinary diversion," *Albanian Journal of Trauma and Emergency Surgery*, vol. 4, no. 2, pp. 679–683, 2020.

[4] Q. Yin, H. Jing, T. Zhu, L. Wu, and L. Yu, "Spatiotemporal evolution characteristics of fluid flow through large-scale 3d rock mass containing filling joints: an experimental and numerical study," *Geofluids*, vol. 2021, Article ID 8883861, 23 pages, 2021.

[5] T. Jiang, L. Ren, J. J. Wang, Z. G. Jia, D. S. Li, and H. N. Li, "Experimental investigation of fiber bragg grating hoop strain sensor–based method for sudden leakage monitoring of gas pipeline," *Structural Health Monitoring*, vol. 20, no. 6, pp. 3024–3035, 2021.

[6] B. A. Naguib, M. M. Ata, M. M. Alzalabani, and B. Yosif, "Performance evaluation and enhancement of apodized fiber bragg grating for dispersion compensation," *AIP Advances*, vol. 11, no. 1, pp. 1–17, 2021.

[7] N. V. Kumar, S. Pant, S. Sridhar, V. Marulasiddappa, and S. Asokan, "Fiber bragg grating based pulse monitoring device for real-time non-invasive blood pressure measurement – a

feasibility study," *IEEE Sensors Journal*, vol. 21, no. 7, pp. 9179–9185, 2021.

[8] N. N. Ismail, M. Sa'Ad, M. F. Ismaila, M. Zaini, and H. Ahmad, "Biaxial 3d-printed inclinometer based on fiber bragg grating technology," *IEEE Sensors Journal*, vol. 21, no. 17, pp. 18815–18822, 2021.

[9] Q. Wang, H. Gao, B. Jiang, H. Yu, and Y. Lv, "Real-time method of obtaining rock mechanics parameters based on the core drilling test," *Geotechnical Testing Journal*, vol. 43, no. 2, pp. 20180080–20180494, 2020.

[10] A. Kerimov, J. Cook, N. Lane, D. Lakshtanov, and G. Gettemy, "Estimating dry rock frame moduli of high-resolution 3d digital rock images using the contact-mechanics-based effective medium approach," *Geophysics*, vol. 85, no. 4, pp. MR235–MR243, 2020.

[11] W. Yang, C. Bo, X. Chen, C. Huang, and G. Li, "Time-dependent behavior of rock-like specimen containing multiple discontinuous joints under uniaxial step-loading compression," *International Journal of Damage Mechanics*, vol. 30, no. 6, pp. 872–898, 2021.

[12] C. Zhang, H. Lin, C. Qiu, T. Jiang, and J. Zhang, "The effect of cross-section shape on deformation, damage and failure of rock-like materials under uniaxial compression from both a macro and micro viewpoint," *International Journal of Damage Mechanics*, vol. 29, no. 7, pp. 1076–1099, 2020.

[13] S. Chen, M. Xiao, and J. Chen, "Failure process and stability analysis of rock blocks in a large underground excavation based on a numerical method," *Mathematical Problems in Engineering*, vol. 2020, no. 6, Article ID 4280428, 12 pages, 2020.

[14] K. Tao and W. Zheng, "An anthropomorphic fuzzy model for the time-spatial assessment of sandstone seepage damage," *Automation in Construction*, vol. 109, no. Jan., article 102989, 2020.

[15] H. Liu, W. Shi, and T. Yang, "Numerical modeling on anisotropy of seepage and stress fields of stratified rock slope," *Mathematical Problems in Engineering*, vol. 2020, no. 4, Article ID 4956025, 10 pages, 2020.

[16] A. Badarch, J. D. Fenton, and T. Hosoyamada, "Application of free-surface immersed-boundary lattice boltzmann method to waves acting on coastal structures," *Journal of Hydraulic Engineering*, vol. 146, no. 2, 2020.

[17] T. Ozaki, A. Wakai, G. Sato, T. Kimura, and A. Watanabe, "Simulation of slope failure distributions due to heavy rain on an island composed of highly weathered granodiorite based on the simple seepage analysis," *Journal of Disaster Research*, vol. 16, no. 4, pp. 626–635, 2021.

[18] X. Wang, J. Chen, J. Zhu, and D. Gong, "Effect of the angle between hydraulic fracture and natural fracture on shale gas seepage," *Mathematical Problems in Engineering*, vol. 2020, no. 2/3, Article ID 5136948, 13 pages, 2020.

[19] M. Lu, Y. Su, Z. Wen, Y. Zhan, and A. Almrabat, "Research on stress alternation effects and fracture reorientation for refracturing treatment," *Simulation*, vol. 97, no. 2, pp. 97–107, 2021.

[20] M. S. Toran, A. D'Haese, I. Rodriguez-Roda, and W. Gernjak, "Fouling propensity of novel tfc membranes with different osmotic and hydraulic pressure driving forces," *Water Research*, vol. 175, no. May15, article 115657, 2020.

[21] M. Fan and A. Sharma, "Design and implementation of construction cost prediction model based on svm and lssvm in industries 4.0," *International Journal of Intelligent Computing and Cybernetics*, vol. 14, no. 2, pp. 145–157, 2021.

[22] J. Jayakumar, S. Chacko, and P. Ajay, "Conceptual implementation of artificial intelligent based e-mobility controller in smart city environment," *Wireless Communications and Mobile Computing.*, vol. 2021, article 5325116, pp. 1–8, 2021.

[23] J. Chen, J. Liu, X. Liu, X. Xu, and F. Zhong, "Decomposition of toluene with a combined plasma photolysis (Cpp) reactor: influence of UV irradiation and byproduct analysis," *Plasma Chemistry and Plasma Processing*, vol. 41, no. 1, pp. 409–420, 2021.

[24] R. Huang, S. Zhang, W. Zhang, and X. Yang, "Progress of zinc oxide-based nanocomposites in the textile industry," *IET Collaborative Intelligent Manufacturing*, vol. 3, no. 3, pp. 281–289, 2021.

[25] Z. Guo and Z. Xiao, "Research on online calibration of lidar and camera for intelligent connected vehicles based on depth-edge matching," *Nonlinear Engineering*, vol. 10, no. 1, pp. 469–476, 2021.